

# Hematite $\alpha\text{-Fe}_2\text{O}_3$ (0001) in Top and Side View: Resolving Long-Standing Controversies about Its Surface Structure

Jesús Redondo,\* Jan Michalička, Florian Kraushofer, Giada Franceschi, Břetislav Šmíd, Nishant Kumar, Ondřej Man, Matthias Blatnik, Dominik Wrana, Benjamin Mallada, Martin Švec, Gareth S. Parkinson, Martin Setvin, Michele Riva, Ulrike Diebold,\* and Jan Čechal\*

Hematite is a common iron oxide found in nature, and the  $\alpha\text{-Fe}_2\text{O}_3$  (0001) plane is prevalent on the nanomaterial utilized in photo- and electrocatalytic applications. The atomic-scale structure of the surface remains controversial despite decades of study, partly because it depends on sample history as well as the preparation conditions. Here, a comprehensive study is performed using an arsenal of surface techniques (non-contact atomic force microscopy, scanning tunneling microscopy, low-energy electron diffraction, and X-ray photoemission spectroscopy) complemented by analyses of the near surface region by high-resolution transmission electron microscopy and electron energy loss spectroscopy. The results show that the so-called “bi-phase” termination forms even under highly oxidizing conditions; a  $(1 \times 1)$  surface is only observed in the presence of impurities. Furthermore, it is shown that the biphasic is actually a continuous layer distorted due to a mismatch with the subsurface layers, and thus not the proposed mixture of  $\text{FeO}(111)$  and  $\alpha\text{-Fe}_2\text{O}_3$  (0001) phases. Overall, the results show how combining surface and cross-sectional imaging provides a full view that can be essential for understanding the role of the near-surface region on oxide surface properties.

to the different crystal structures and stoichiometries of iron and oxygen in various compounds.<sup>[1]</sup> Hematite ( $\alpha\text{-Fe}_2\text{O}_3$ ) has attracted much attention in green chemistry due to its abundance and low toxicity,<sup>[2]</sup> as well as its 1.9–2.2 eV bandgap, which permits electronic excitation by visible light.<sup>[3–5]</sup> Nevertheless, the efficiency of water splitting on hematite is well below the predicted (and industrially required) 15% solar-to-hydrogen conversion.<sup>[6]</sup> Sixty years of research has led to the consensus that the reactivity is governed by electronic states formed at the oxide/electrolyte interface.<sup>[7]</sup> However, the origin, amount, and role of these states remains a matter of controversy.<sup>[8,9]</sup> A comprehensive understanding of the surface structure is crucial for the identification of active surface sites, while reaction-limiting factors such as light-depth penetration and charge-carrier trapping and recombination are inherently linked to the


subsurface and bulk properties.<sup>[10,11]</sup> In recent years, attention has been paid to the characterization of bulk phenomena such as polaron formation and electron-hole recombination<sup>[12–14]</sup> and

## 1. Introduction

Iron oxides are extensively studied thanks to their wide-ranging electronic, magnetic, and catalytic properties, which arise due

J. Redondo, B. Šmíd, D. Wrana, M. Setvin  
Faculty of Mathematics and Physics  
Charles University  
V Holešovičkách 2/747, Prague, Praha 18000, Czech Republic  
E-mail: redondo@karlov.mff.cuni.cz

J. Redondo  
Faculty of Chemistry  
University of the Basque Country  
Paseo Manuel Lardizabal 3, Donostia-San Sebastián, Guipuzkoa 20018, Spain

 The ORCID identification number(s) for the author(s) of this article can be found under <https://doi.org/10.1002/admi.202300602>

© 2023 The Authors. Advanced Materials Interfaces published by Wiley-VCH GmbH. This is an open access article under the terms of the Creative Commons Attribution License, which permits use, distribution and reproduction in any medium, provided the original work is properly cited.

DOI: 10.1002/admi.202300602

J. Michalička, N. Kumar, O. Man, M. Blatnik, J. Čechal  
Central European Institute of Technology  
Brno University of Technology  
Purkyňova 123, 61200 Brno, Czech Republic  
E-mail: cechal@fme.vutbr.cz

F. Kraushofer, G. Franceschi, G. S. Parkinson, M. Riva, U. Diebold  
Institute of Applied Physics  
Technische Universität Wien  
Wiedner Hauptstraße 8-10/E134, 1040 Vienna, Austria  
E-mail: diebold@iap.tuwien.ac.at

D. Wrana  
Marian Smoluchowski Institute of Physics  
Jagiellonian University  
Prof. Stanisława Łojasiewicza 11, 30-348 Krakow, Poland  
B. Mallada, M. Švec  
Institute of Physics  
Czech Academy of Science  
Na Slovance 2, 18200 Prague, Czech Republic

the effect of the bulk morphology on the final reaction yield.<sup>[15,16]</sup> The fundamental investigation of the redox behavior of hematite and its surface structures can provide important feedback for a better understanding of actual catalytic reactions.

Hematite  $\alpha$ -Fe<sub>2</sub>O<sub>3</sub>(0001), hereafter Fe<sub>2</sub>O<sub>3</sub> for simplicity, has been extensively investigated in fundamental and applied research. If a sample is prepared under sufficiently oxidizing anhydrous conditions ( $\mu_o > -1.8$  eV), Fe<sub>2</sub>O<sub>3</sub> is the stable bulk phase and the surface is reported to exhibit a (1 × 1) periodicity.<sup>[17]</sup> Several competing models have been proposed for the structure, including the O<sub>3</sub>–, OH–Fe–, and “half-metal” terminations.<sup>[18,19]</sup>

Such conditions are difficult to combine with the ultrahigh vacuum (UHV) environment utilized in surface science investigations, so many experiments have focused on reducing conditions in the range  $-2.5$  eV  $< \mu_o < -1.8$  eV. Here, magnetite (Fe<sub>3</sub>O<sub>4</sub>) maghemite ( $\gamma$ -Fe<sub>2</sub>O<sub>3</sub>), and  $\alpha$ -Fe<sub>2</sub>O<sub>3</sub> compete as the stable bulk phase,<sup>[20,21]</sup> and the  $\alpha$ -Fe<sub>2</sub>O<sub>3</sub>(0001) surface forms a long-range ordered structure. This is commonly referred to as the “biphase” reconstruction, so-called because it was interpreted as alternating domains with FeO and Fe<sub>2</sub>O<sub>3</sub>.<sup>[22]</sup> This reconstruction has been identified in two structurally similar variants, the “oxygen-poor” (O-poor) and “oxygen-rich” (O-rich) biphase, depending on the preparation conditions in UHV.<sup>[23,24]</sup> The biphase model competes with the earlier FeO<sub>x</sub> overlayer proposed by Lad and Henrich<sup>[25]</sup> and the later Fe<sub>3</sub>O<sub>4</sub>-like overlayer interpretation by Lanier et al.<sup>[26]</sup> Recently, some of the present coauthors introduced an alternative explanation; the “honeycomb model”. This model builds up in the earlier “overlayer” works and proposes a TMD-like FeO<sub>2</sub> structure.<sup>[27]</sup> Finally, if a sample is treated at a low oxygen chemical potential, i.e.,  $\mu_o < -2.5$  eV, or in the presence of a reducing agent, the  $\alpha$ -Fe<sub>2</sub>O<sub>3</sub>(0001) surface is readily reduced to Fe<sub>3</sub>O<sub>4</sub>(111).<sup>[28]</sup> Equilibrating (i.e., annealing under appropriate O<sub>2</sub> partial pressures) at  $\mu_o > -2.5$  eV initiates the stoichiometric recovery toward Fe<sub>2</sub>O<sub>3</sub>.

The coexistence of different bulk stoichiometries and surface phases on single crystals in UHV makes it difficult to obtain well-defined samples.<sup>[1]</sup> Mixed bulk and surface iron oxide phases can be misidentified due to similarities in their spectral signatures, such as the Fe 2p Fe<sup>3+</sup> satellite structures of Fe<sub>2</sub>O<sub>3</sub> and  $\gamma$ -Fe<sub>2</sub>O<sub>3</sub> in X-ray photoemission spectroscopy (XPS)<sup>[29]</sup> or their pre-peak feature at the Fe 2p L<sub>3</sub> edge in X-ray absorption spectroscopy.<sup>[30]</sup> Thus, a combination of real- and reciprocal-space imaging is required to ensure the existence of a single surface phase.<sup>[27]</sup> Moreover, the presence of natural dopants (Na, Mg, K, Ca, Ti, V, Cr) in commercially available natural hematite crystals can shift the thermodynamic stability window of bulk hematite phases.<sup>[31]</sup> Foreign impurities can also stabilize new surface phases. For example, K and Ti doping promotes (3 × 2) and (2 × 1) surface reconstructions on Fe<sub>2</sub>O<sub>3</sub>(1 $\bar{1}$ 02) for oxygen chemical potentials at which the (1 × 1) bulk reconstruction occurs in pristine hematite.<sup>[32,33]</sup> Sample impurities have also been linked to the (1 × 1) termination of Fe<sub>2</sub>O<sub>3</sub><sup>[34]</sup> and  $\alpha$ -Al<sub>2</sub>O<sub>3</sub>(0001).<sup>[35]</sup>

The rich chemistry of hematite requires analyzing the bulk and surface of iron oxide not as separated entities but as closely interrelated systems.<sup>[6]</sup> In this work, we address the current challenges using  $\alpha$ -Fe<sub>2</sub>O<sub>3</sub>(0001) as a model system for UHV investigations,<sup>[36]</sup> and tackle the controversy over the nature of the honeycomb/biphase reconstruction. We monitor the structural and chemical evolution of the bulk and surface of Fe<sub>2</sub>O<sub>3</sub>

single crystals at different anhydrous redox conditions, also emphasizing the role of natural impurities. We characterize the surface of Fe<sub>2</sub>O<sub>3</sub> by STM, non-contact atomic force microscopy (nc-AFM), low-energy electron diffraction (LEED), and XPS. We have investigated the evolution of surface reconstructions on natural and synthetic Fe<sub>2</sub>O<sub>3</sub> crystals and disentangled the effect of sample impurities on their stability. We utilize high-resolution transmission electron microscopy (HRTEM) and electron energy loss spectroscopy (EELS) to provide a view of the near-surface bulk phases of Fe<sub>2</sub>O<sub>3</sub> single crystals with sub-nanometer resolution. Employing nc-AFM, we found that the honeycomb/biphase Fe<sub>2</sub>O<sub>3</sub> surface phase is formed by a compact 2D layer whose structure is locally perturbed. This local perturbation gives rise to the areas of distinct contrast identified as a “biphase” in previous works.<sup>[22,37]</sup>

## 2. Results and Discussion

### 2.1. Hematite Bulk Oxidation

The near-surface bulk of Fe<sub>2</sub>O<sub>3</sub> is significant for on-surface catalytic reactions as it can store defects, host electron–hole pair creation and their transport to the surface, or determine the penetration depth of light. In particular, the reoxidation process of hematite is relevant in photo- and electrocatalytic reactions that involve oxygen exchange or iron redox cycles (e.g., during the water-shift reaction where a redox cycle of Fe<sup>3+</sup> to Fe<sup>2+</sup> takes place). If the surface or near-surface region of hematite is reduced toward Fe<sub>3</sub>O<sub>4</sub> or FeO the reoxidation process is critical to maintain catalyst activity over many reaction cycles. Model hematite systems used for UHV investigations lack information on the extent to which the bulk transforms when equilibrating at different oxygen chemical potentials. Mixed bulk phases and the interface between bulk hematite and surface phases cannot be probed by surface-sensitive techniques. To fully describe the surface, one needs information about the near-surface bulk structure.

Bulk phases of hematite thin films grown on polar oxides can be probed by HRTEM.<sup>[38]</sup> Here, HRTEM is used to access cross-sectional information on the sub-surface region of  $\alpha$ -Fe<sub>2</sub>O<sub>3</sub>(0001) single crystals. Two limiting cases are presented: one sample featuring the Fe<sub>3</sub>O<sub>4</sub>(111) phase ( $\mu_o < -2.5$  eV) and one the fully oxidized Fe<sub>2</sub>O<sub>3</sub> phase ( $\mu_o > -1.8$  eV). As a technical note, the study of the sub-surface microstructure by TEM requires an electron-transparent specimen cut from the sample (a lamella). The fabrication of lamellas and the procedure to avoid surface contamination in the process is detailed in the experimental section.

The HRTEM images of the reduced sample (Figure 1a,b) show the near-surface structure of the Fe<sub>3</sub>O<sub>4</sub>(111)-terminated Fe<sub>2</sub>O<sub>3</sub>. Two distinct regions are divided by a sharp interface. The first region is a surface layer that can be identified as a Fe<sub>3</sub>O<sub>4</sub> lattice oriented to the zonal axis (i.e., parallel to the electron beam) [112], Figure 1c, by evaluation of FFT and crystallographic standard.<sup>[39]</sup> Note that HRTEM cannot unambiguously distinguish the lattice of Fe<sub>3</sub>O<sub>4</sub> from  $\gamma$ -Fe<sub>2</sub>O<sub>3</sub> due to their similar inverse cubic spinel crystal structure and lattice parameter. Therefore, we subsequently introduced an EELS analysis to discern between these two structures. The second region is a single-crystalline bulk with a dumbbell atomic pattern identified as the rhombohedral lattice of Fe<sub>2</sub>O<sub>3</sub> hematite oriented to the zonal axis [1120], Figure 1d,



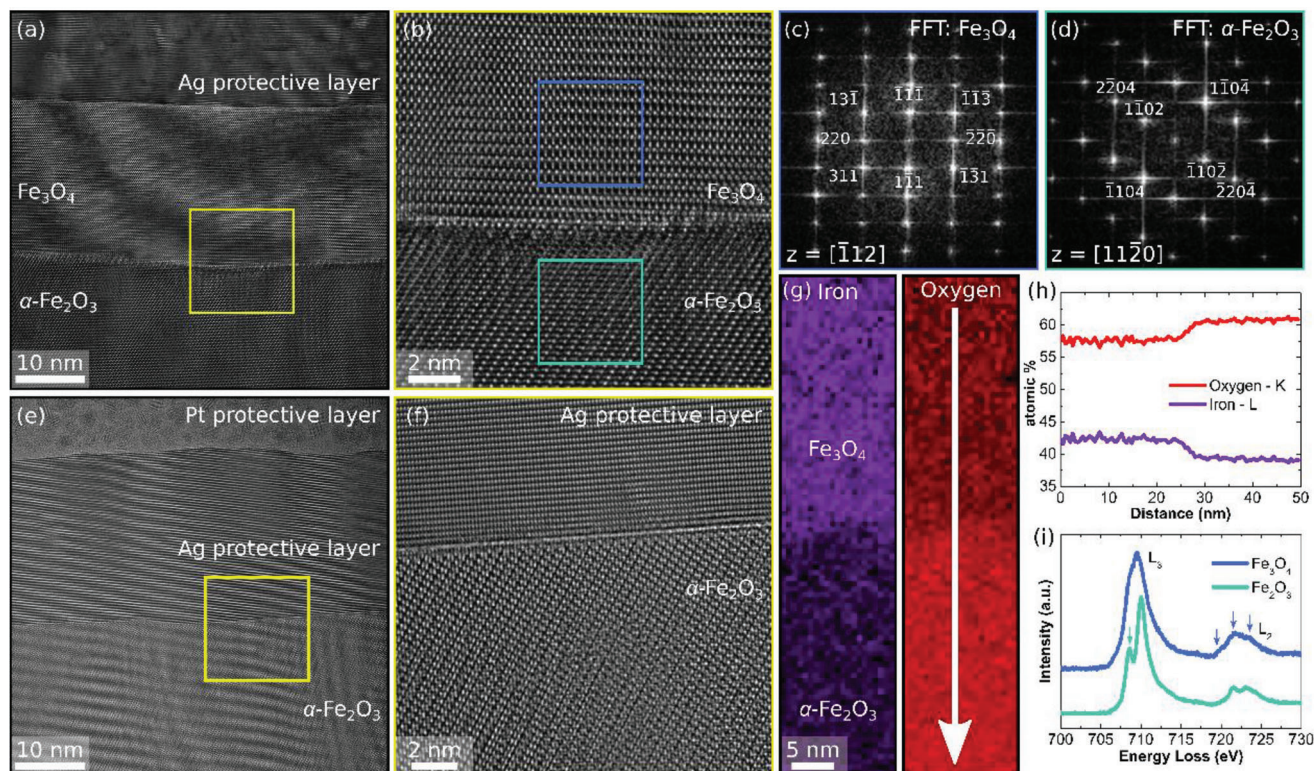


**Figure 1.** Reduced and oxidized hematite in side view. a,b) HRTEM images of the partially reduced hematite showing an  $\text{Fe}_3\text{O}_4$  magnetite film on  $\text{Fe}_2\text{O}_3$  hematite substrate. The magnetite and hematite are oriented to the zonal axis  $[\bar{1}12]$  and  $[11\bar{2}0]$ , respectively, as revealed by FFT analysis in (c,d). e,f) HRTEM images of the fully oxidized sample revealing a single crystal structure identified by FFT as  $\text{Fe}_2\text{O}_3$  hematite oriented to the  $[11\bar{2}0]$  zonal axis. The dumbbell atomic structure characteristic of  $\alpha\text{-Fe}_2\text{O}_3$  (0001) appears undisturbed all the way up the interface with the Ag protective layer. g) STEM-EELS atomic concentration maps associated with Fe-L<sub>2,3</sub> and O-K edges of the magnetite-hematite interface. h) Fe and O relative atomic concentration measured by EELS along the white arrow in (g). i) Monochromated STEM-EELS spectra of Fe-L<sub>2,3</sub> fine-edge structure measured on the partially reduced sample in the bulk (cyan) and in the reduced layer closer to the surface (blue curve). The blue arrows mark the three  $L_2$  components arising from the three Fe sites in magnetite (octahedral  $\text{Fe}^{2+}$  and  $\text{Fe}^{3+}$  and tetrahedral  $\text{Fe}^{3+}$ ). The cyan arrow indicates the position of the  $L_3$  pre-peak arising from the spin-orbit splitting of the 2p orbital.

by evaluation of FFT and crystallographic standard.<sup>[40]</sup> Along the whole length of the lamella, the surface layer reveals a defect-free single crystal structure without fragmentation to misoriented sub-grains. The thickness of the surface layer is  $\approx 20\text{--}25$  nm. This thickness generally depends on the degree of reduction of the sample, i.e., by the ion beam energy, total sputtering dose, and the duration of UHV-annealing treatments prior to cutting the lamellae. The HRTEM analysis of the fully reoxidized sample given in Figure 1e,f reveals that  $\text{Fe}_2\text{O}_3$ , again identified by FFT evaluation (not shown) and crystallographic standard, is present up to the surface, forming an atomically sharp interface with the Ag protective layer. This indicates that full oxidation of the sample can be achieved at  $\mu_0 > -1.8$  eV even in a UHV chamber.

EELS mapping performed in scanning-TEM mode (STEM-EELS) provides spatially resolved information about the chemical composition, oxidation, and valence states of the investigated iron oxides.<sup>[41]</sup> Figure 1g shows the EELS atomic concentration maps associated with Fe-L and O-K edges obtained from the quantification of a spectrum image at the Ag-buried interface. The relative Fe and O concentration as a function of depth (along the arrow in Figure 1g) is shown in Figure 1h. The deeper bulk part shows a 40:60 Fe:O ratio, while a 43:57 ratio is measured

in the upper surface layer. These values correspond well to the nominal stoichiometries expected for  $\text{Fe}_2\text{O}_3$  (40:60) and  $\text{Fe}_3\text{O}_4$  (42.9:57.1), respectively. Figure 1i shows monochromated STEM-EELS spectra of the Fe-L<sub>2,3</sub> fine-edge structure measured in both bulk (cyan curve) and reduced (blue curve) regions of the same sample. The bulk spectrum shows a strong pre-peak  $L_3$  component (cyan arrow) and two  $L_2$  main contributions, whereas the upper layer shows no  $L_3$  pre-peak and three  $L_2$  contributions (blue arrows). These spectra are consistent with those expected for  $\text{Fe}_2\text{O}_3$  and  $\text{Fe}_3\text{O}_4$ , respectively.<sup>[42]</sup> The combination of TEM and EELS structural and chemical analyses excludes the presence of  $\gamma\text{-Fe}_2\text{O}_3$ , and reveals the formation of a surface  $\text{Fe}_3\text{O}_4$  layer with a well-defined interface on the  $\text{Fe}_2\text{O}_3$  bulk structure under the conditions of controlled UHV experiments.

## 2.2. Overview of the Previously Reported Surface Reconstructions

In combination with the bulk configuration, the initial structure and evolution of the surface of hematite determines the performance of a photoelectrocatalytic reaction (e.g., via the amount

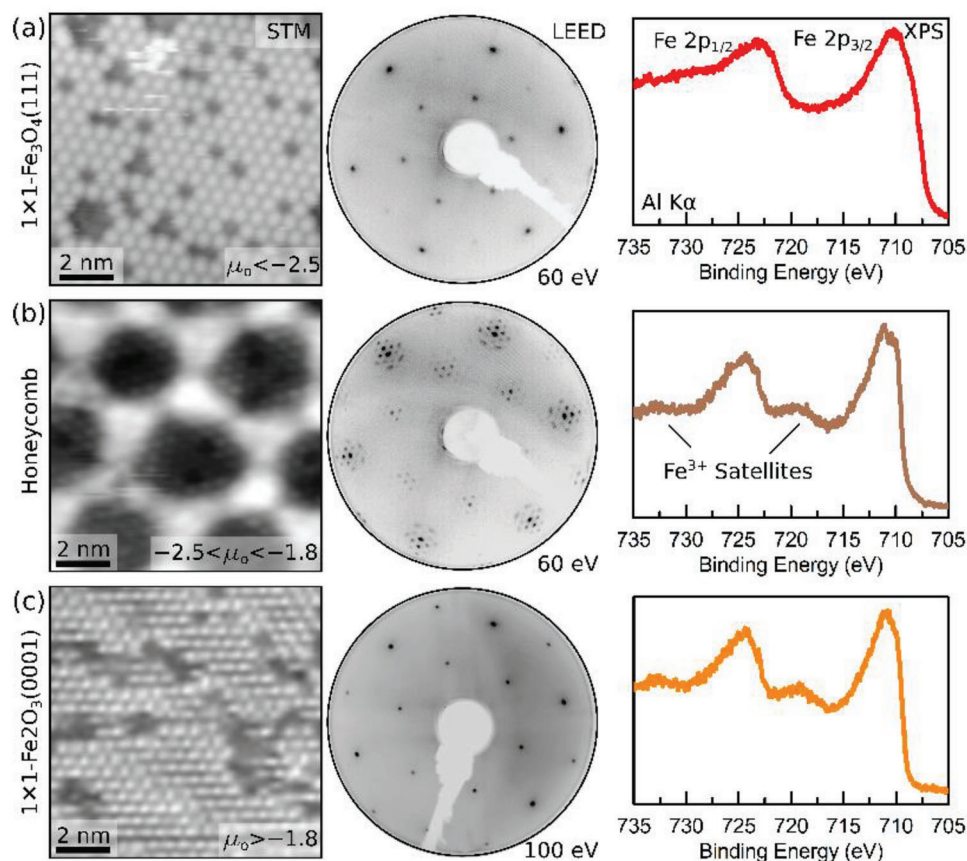


**Figure 2.** Surface reconstructions of  $\alpha'$ - $\text{Fe}_2\text{O}_3$  (0001) natural crystals at different oxygen chemical potentials ( $\mu_o$ ). Representative room-temperature STM, LEED, and XPS results for a) the  $(1 \times 1)$ - $\text{Fe}_3\text{O}_4(111)$  reconstruction obtained at  $\mu_o < -2.5$  eV; b) the O-rich honeycomb (biphase) reconstruction in the range  $-2.5$  eV  $< \mu_o < -1.8$  eV. STM and LEED reveal a complex Moiré pattern; c) the bulk-like termination of  $\text{Fe}_2\text{O}_3$  at  $\mu_o > -1.8$  eV. STM parameters: a)  $-0.5$  V,  $0.5$  nA, b)  $1.5$  V,  $0.6$  nA, and c)  $1$  V,  $3$  nA. LEED: The pattern in (c) was obtained from a different sample than (a) and (b); the sample was mounted on the sample plate with a different orientation. XPS:  $E_{\text{pass}} = 20$  eV, Al  $K\alpha$  X-ray source, normal emission.

and type of surface states). **Figure 2** shows an overview of individual surface reconstructions typically found on (0001)-oriented  $\text{Fe}_2\text{O}_3$  natural single crystals under different oxygen chemical potentials in anhydrous conditions. They are commonly referred in the literature as a)  $(1 \times 1)$ - $\text{Fe}_3\text{O}_4(111)$ , b) honeycomb/biphase, and c)  $(1 \times 1)$ - $\text{Fe}_2\text{O}_3(0001)$  phases. This nomenclature refers to the magnetite and hematite periodicities relative to the periodicity of the iron layers. Instead, sometimes the periodicities are specified relative to the oxygen basal planes in the literature; namely  $(2 \times 2)$ - $\text{Fe}_3\text{O}_4(111)$  and  $(\sqrt{3} \times \sqrt{3})R30^\circ$ - $\text{Fe}_2\text{O}_3(0001)$ . The  $(1 \times 1)$ - $\text{Fe}_3\text{O}_4(111)$  phase, Figure 2a, is obtained when samples are treated under reducing conditions. It results from preferential sputtering of O atoms and subsequent annealing in UHV ( $\mu_o < -2.5$  eV).<sup>[1]</sup>  $\text{Fe}_3\text{O}_4(111)$  may terminate at up to six different possible layer cuts, of which the  $\text{Fe}_{\text{tet}}$  bulk termination displayed in Figure 2a is the most stable as the single phase at  $\mu_o = -2.5$  eV.<sup>[43]</sup> LEED shows the corresponding diffraction pattern. The Fe 2p XPS spectrum lacks the  $\text{Fe}^{3+}$  satellite peaks characteristic of  $\text{Fe}_2\text{O}_3$ <sup>32</sup> and shows a distinctive broad  $2p_{3/2}$  component due to a mixture of  $\text{Fe}^{2+}$  and  $\text{Fe}^{3+}$  multiplet peaks. The honeycomb/biphase reconstruction has been reported to occur in two variants, the O-poor and O-rich biphase, where the O-rich phase contains only  $\text{Fe}^{3+}$  ions while the O-poor phase also

contains some  $\text{Fe}^{2+}$ .<sup>[23,24]</sup> Figure 2b shows the fingerprints of the O-rich honeycomb/biphase reconstruction, which results from annealing in oxygen between  $\mu_o = -2.5$  and  $-1.8$  eV. This surface displays complex tip-dependent STM contrasts and a floretted LEED pattern arising from the Moiré superstructure formed by the  $\text{Fe}_2\text{O}_3$  substrate and a  $\text{FeO}$  overlayer.<sup>[27]</sup> The associated Fe 2p XPS signal develops  $\text{Fe}^{3+}$  satellites and a sharper  $\text{Fe} 2p_{3/2}$  component. Figure S1 (Supporting Information) shows a comparison with the O-poor honeycomb/biphase, obtained by annealing the O-rich variant in reducing conditions.<sup>[23]</sup> At higher  $\mu_o$ ,  $\text{Fe}_2\text{O}_3$  natural crystals exhibit instead a  $(1 \times 1)$  periodicity, Figure 2c. The LEED pattern of the  $(1 \times 1)$  phase shows only the main spots. The Fe 2p lineshape from the  $(1 \times 1)$  phase shows  $\text{Fe}^{3+}$  satellites typical of stoichiometric hematite.

### 2.3. Is the Honeycomb Structure a True Biphase?

The controversy around the biphase versus overlayer models has its foundation in the complex STM contrast shown in Figure 2b, which has often been interpreted as a coexistence of multiple distinct structural phases ( $\text{FeO}$  and  $\text{Fe}_2\text{O}_3$ ).<sup>[22]</sup> To address this controversy, nc-AFM measurements at 78 K were performed.



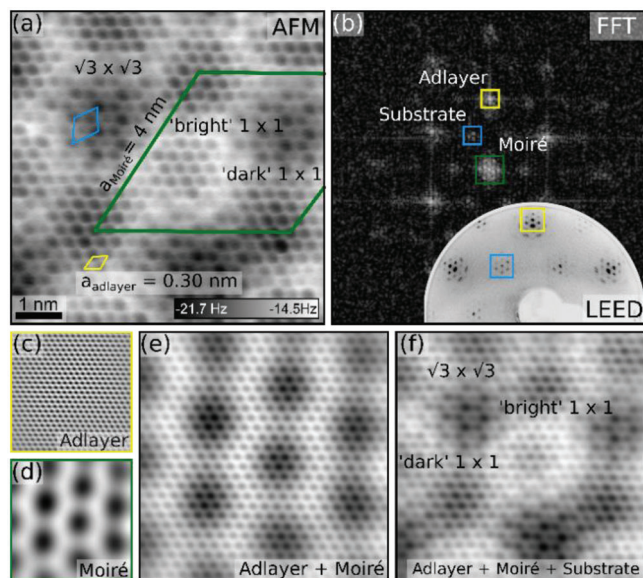


**Figure 3.** Analysis of the honeycomb phase with constant-height nc-AFM. a) Atomically-resolved image (8 nm × 8 nm). Atoms are imaged in the attractive regime (dark contrast). b) FFT of the image shown in (a). The yellow, blue, and green squares highlight the (1 × 1) ( $\sqrt{3} \times \sqrt{3}$ ) and Moiré periodicities found in the real space, respectively. The inset shows a LEED pattern of the same surface reconstruction. c,d) Adlayer and Moiré components of the nc-AFM image extracted from (b) by inverse FFT. e) Composition made by adding (c) and (d), showing an AFM contrast reminiscent of a Moiré pattern. f) Composition obtained by adding the substrate contribution (blue) to (e).

**Figure 3a** shows an atomically resolved, constant-height image of the O-rich honeycomb phase. Individual atoms, imaged as dark circles, are arranged with a periodicity of  $0.30 \pm 0.01$  nm (yellow rhombus). This basic structural motif is modulated on a large scale forming the  $4 \pm 0.1$  nm honeycomb superstructure (green rhombus). Within the superstructure, three areas have a distinct appearance. These are marked as ( $\sqrt{3} \times \sqrt{3}$ ), “bright” (1 × 1), and “dark” (1 × 1). The fast Fourier transform (FFT) shown in **Figure 3b** gives an additional  $0.52 \pm 0.03$  nm periodicity, which is most apparent within the ( $\sqrt{3} \times \sqrt{3}$ ) region (blue rhombus). The unit cell vector with length of 0.52 nm corresponds to the hematite substrate.

The LEED pattern in **Figure 2b** and the FFT in **Figure 3b** are strikingly reminiscent of a Moiré structure. It arises from the existence of a large periodicity, as revealed by the nc-AFM contrast in **Figure 3a**. Previous work<sup>[27]</sup> attributed the presence of one ( $\sqrt{3} \times \sqrt{3}$ ) and two (1 × 1) domains in the STM images to differences in atomic heights of the last O layer of FeO<sub>2</sub>, according to the overlayer placement on the substrate.<sup>[27]</sup> Similarly, the Fe<sub>3</sub>O<sub>4</sub>-like overlayer model proposed by Lanier et al. produces three distinct domains according to the coordination (octahedral, tetrahedral, and non-standard six-coordinated) of the Fe atoms in the surface layer.<sup>[26]</sup> However, the different domains could also arise from electronic effects due to different tunneling between tip and sample at different sites.<sup>[37]</sup> The nc-AFM images support the overlayer scenario. They were obtained in constant height mode (high sensitivity to sub-nanometer atomic-height variations) at the contact potential difference between tip and sample. At these condi-

tions, Pauli and van der Waals interactions (electrostatic contributions) are minimized. Moreover, since hematite is insulating at the acquisition temperature of 78 K, there is no tunneling current between tip and sample. Thus, the measured contrast should largely arise from slight atomic height differences along the honeycomb superstructure, which strongly supports the topographic origin of the AFM (and STM) contrast in favor of an overlayer model. **Figure 3c,d** show a decomposition of the nc-AFM image in the adlayer (yellow) and Moiré (green) components of the FFT of **Figure 3b**. The combination of Moiré and adlayer contributions in **Figure 3e** produces an image typical for supported 2D materials.<sup>[44]</sup> Adding the substrate contribution to Moiré plus adlayer composition produces the ( $\sqrt{3} \times \sqrt{3}$ ) and two (1 × 1) fine modulations, given in **Figure 3f**. The ( $\sqrt{3} \times \sqrt{3}$ ) and (1 × 1) areas can be, in principle, identified as “domains” with distinct local structure and chemistry (the local differences in AFM contrast indicate different tip–sample chemical forces), but not in the extent considered within the biphasic model (alternating islands of different stoichiometry, FeO and Fe<sub>2</sub>O<sub>3</sub>).

The STM and LEED of the O-poor honeycomb/biphase reported in **Figure S1** (Supporting Information) also resembles the prototypical Moiré pattern of an overlayer structure. The Fe<sup>2+</sup> fingerprints observed in its corresponding XPS Fe 2p lineshape are in good agreement with data reported by Lanier et al.<sup>[26]</sup> and would support an Fe<sub>3</sub>O<sub>4</sub>-like stoichiometry of the overlayer, as proposed by these authors. Likewise, the fully-oxidized Fe 2p lineshape shown in **Figure 2b** for the O-rich biphasic points toward a stoichiometry close to Fe<sub>2</sub>O<sub>3</sub>, in line with previous FeO<sub>x</sub> models.<sup>[25,27]</sup> The evidence shown here strongly hints toward two similar overlayer structures for the honeycomb/biphase reconstruction, which differ in the exact stoichiometry and attachment to the underlying substrate.

#### 2.4. Relative Stability of Honeycomb Structure and (1 × 1)-Fe<sub>2</sub>O<sub>3</sub>(0001): The Role of Impurities

The (1 × 1)-Fe<sub>2</sub>O<sub>3</sub>(0001) atomic termination at high values of  $\mu_0$ , **Figure 2c**, is also subject to some controversy. The [0001] direction of hematite has a polar alternation of Fe and O planes. Based on the autocompensation mechanism, only a stoichiometric Fe-terminated surface would be consistent with non-polarity under UHV conditions.<sup>[45,46]</sup> However, (1 × 1) O–, Fe–, OH– and mixed terminations have been reported for samples prepared in UHV and near-ambient pressure (NAP).<sup>[1,47]</sup> It has been hinted that their stability might be linked to the metallic support used to grow Fe<sub>2</sub>O<sub>3</sub> films.<sup>[18]</sup> Hematite single crystals can be considered as a quasi-infinite system on which autocompensation must happen at a vacuum-exposed surface. On supported oxide thin films, this can occur at the metal-oxide interface, providing more degrees of freedom for surface terminations. Another possibility is that the surface structure is altered by natural or incorporated impurities.<sup>[34]</sup> The (1 × 1) termination has been reported to form on both natural and synthetic single crystals.<sup>[48]</sup> However, it cannot be ruled out that the (1 × 1) forms due to impurities (e.g., adventitious carbon and water) adsorbed during air transport to the measuring instruments. Natural impurities or added dopants such as K and Ti are known to induce surface restructuring on  $\alpha$ -Fe<sub>2</sub>O<sub>3</sub>(1102).<sup>[32,33]</sup>

**Table 1.** Summary of surface structures obtained when equilibrating natural and synthetic  $\text{Fe}_2\text{O}_3$  at different oxygen chemical potentials. The honeycomb-to- $(1 \times 1)$  transition occurs at a  $\mu_o \approx -1.8$  eV only on natural samples; however, the precise value depends on the specific sample.

$\mu_o$ [eV]	Natural	Synthetic	$p$ (mbar)	T [°C]
-2.22	Honeycomb	Honeycomb	$1 \times 10^{-9}$	700
-2.04	Honeycomb	Honeycomb	$1 \times 10^{-5}$	800
-1.94	Honeycomb	Honeycomb	$1 \times 10^{-6}$	700
-1.84	Honeycomb	Honeycomb	$1 \times 10^{-5}$	700
-1.74	$(1 \times 1)$ $\alpha\text{-Fe}_2\text{O}_3$ (0001)	Honeycomb	$1 \times 10^{-4}$	700
-1.63	$(1 \times 1)$ $\alpha\text{-Fe}_2\text{O}_3$ (0001)	Honeycomb	$1 \times 10^{-5}$	600
-0.92	$(1 \times 1)$ $\alpha\text{-Fe}_2\text{O}_3$ (0001)	Honeycomb	$1 \times 10^{-4}$	300
-0.77	$(1 \times 1)$ $\alpha\text{-Fe}_2\text{O}_3$ (0001)	Honeycomb	0.5	300
-0.55	$(1 \times 1)$ $\alpha\text{-Fe}_2\text{O}_3$ (0001)	Honeycomb	0.5	150

To disentangle the effects of sample impurities from other effects on given surface reconstructions, natural and synthetic  $\text{Fe}_2\text{O}_3$  samples were prepared and investigated in UHV, using typical ranges of pressure and temperature found in the literature for the preparation of the honeycomb and  $(1 \times 1)\text{-Fe}_2\text{O}_3(0001)$  phases. The amount and type of impurities in natural crystals vary with each sample. Common impurities detected by XPS were alkali metals such as Ca, K, and Na, and transition metals such as Ti, Mn, and Cr. Clean, epitaxial thin films of  $\approx 100$  nm thickness were grown by pulsed laser deposition (PLD) on natural hematite single crystals,<sup>[33]</sup> henceforth referred to as “synthetic” hematite. These films are free from impurities within the resolution limit of the XPS setup. **Table 1** shows the range of chemical potentials probed in this work when oxygen-annealing natural and synthetic  $\alpha\text{-Fe}_2\text{O}_3(0001)$  samples. Natural crystals exhibit the honeycomb surface reconstruction when treated under reducing conditions and the  $(1 \times 1)\text{-Fe}_2\text{O}_3(0001)$  termination under oxidizing conditions. The phase transition between honeycomb and  $(1 \times 1)\text{-Fe}_2\text{O}_3(0001)$  on natural crystals fits well with the  $\mu_o$  values reported for these phases on metal-supported hematite and natural crystals. On synthetic samples, however, only the honeycomb reconstruction was obtained; the  $(1 \times 1)\text{-Fe}_2\text{O}_3(0001)$  termination could not be reproduced within common pressure and temperature ranges. What is more, the growth kinetics and time used for equilibration of the honeycomb phase depends on  $\mu_o$ . To obtain the honeycomb phase from the  $\text{Fe}_3\text{O}_4$ -terminated hematite within UHV-compatible oxygen pressures ( $p < \approx 10^{-4}$  mbar), annealing between 2 and 8 h is typically required (the exact duration depends on the history of the sample). However, merely 10–30 min are required under high oxygen pressure ( $\approx 1$  mbar).

## 2.5. Impurity Segregation during Hematite Oxidation

The effect of the intrinsic impurities of natural crystals not only affects the stability of surface reconstructions of  $\alpha\text{-Fe}_2\text{O}_3(0001)$  but also the bulk transformations and the fully stoichiometric recovery of hematite. Earlier works by Chiaramonti et al. demonstrate the occurrence of ferrite spinel phases on the near-surface of hematite  $\text{Fe}_2\text{O}_3$  upon  $\text{Ar}^+$  bombardment.<sup>[31]</sup> Such phases could only be obtained on natural crystals containing minute amounts of impurities. Figure S2a (Supporting Information) shows an

HRTEM image of a partially reoxidized magnetite-like inclusion within the fully recovered hematite. FFT analysis of the inclusion and the surrounding area, Figure S2b,c, (Supporting Information) reveals that the inclusion has the same magnetite/maghemite structure as shown in Figure 3c, whereas the rest of the bulk has the characteristic hematite structure. The EELS mapping in Figure S2d,e (Supporting Information) reveals an inhomogeneous presence of Mn in the 6–12% range. The Fe concentration is locally decreased by an equivalent amount. O concentration is decreased only to a degree expected for magnetite. The  $\text{Fe-L}_{2,3}$  edge structure of the inclusion, Figure S3 (Supporting Information), resembles that of magnetite reported in Figure 1i. This evidence suggests the formation of  $\text{Fe}_{3-x}\text{Mn}_x\text{O}_4$  ferrite. Outside the inclusion, the Mn concentration is below the detection limit of EELS. The interplanar-spacing vector lengths of the Mn-rich area are shown in Table ST1 (Supporting Information). Mn locally hinders the full reoxidation of the sample at oxygen chemical potentials at which fully stoichiometric hematite is obtained on clean samples. Moreover, Mn single dopants alter the hole mobility in hematite<sup>[49]</sup> and, depending on the Mn concentration and sample preparation parameters, Mn possibly could lead to ferrite or Mn oxide formation. It is also likely that minute amounts of impurities such as Mn can distribute all over the hematite surface, resulting in a  $(1 \times 1)$  bulk-like termination.

These results confirm that impurities play a crucial role in changing the thermodynamic balance of the hematite surface and near-surface structure and chemistry. The formation of ferrite-like structures embedded in hematite occurs all the way from reducing conditions<sup>[31]</sup> to the oxidizing parameters used to fully recover hematite. During the reoxidation, the impurities are pushed out, thus changing the surface and near-surface composition and chemistry. The concentration and elemental distribution of contaminants vary within each natural crystal and preparation. Hence, synthetic films are essential for an adequate characterization of hematite in catalysis.

## 3. Conclusion

This work addressed the structure of the hematite  $\alpha\text{-Fe}_2\text{O}_3(0001)$  surface and near-surface. High-resolution nc-AFM images acquired in UHV strongly support that the oxidized surface of hematite is natively composed of a 2D oxide layer. The layer shows a Moiré pattern with three different areas due to the

distinct attachment to the underlying fully oxidized bulk; these areas are responsible for the “biphase” contrast observed in STM. A series of controlled experiments compared the oxidation of synthetic films with natural crystals, the former clean within the resolution limit of XPS and the latter contaminated by intrinsic impurities. The surface termination is strongly influenced by the presence of impurities, forcing the formation of surface phases that are not thermodynamically preferred on a clean sample. Specifically, the presence of impurities (e.g., alkali metals) enforces the formation of a  $(1 \times 1)$ - $\text{Fe}_2\text{O}_3$ (0001) termination instead of the honeycomb one in a wide range of oxygen chemical potentials. Finally, subsurface cross-sectional analysis by TEM reveals the spatial extent of changes introduced by surface preparation methods and the spatial localization of impurities that can be associated with a particular ferrite phase.

The atomic structure and transformations of  $\alpha$ - $\text{Fe}_2\text{O}_3$ (0001) during actual catalytic reactions are generally poorly understood.<sup>[36]</sup> The effect of impurities/dopants in the surface reactivity can be complex and would depend on their type and concentration as well as the specific reaction and reaction conditions. Impurities significantly influence the structure and chemistry of both the hematite surface and its bulk. This is of relevance in photoelectrocatalysis (water splitting, Fenton process, Fischer-Tropsch reaction), which typically uses alkali-containing electrolytes (e.g., KOH, NaOH, and carbonates) and metal-doped hematite (e.g., Ti, Zn, Mn, Ni) to improve conductivity and charge separation. The present study shows how hematite surfaces are rich and complex even in the simplest approximation (UHV and anhydrous conditions). Under more realistic photo- and electrocatalytic conditions, metallic dopants, surface (oxy)hydroxylation, and/or cation adsorption will play a crucial role in achieving a non-polar, stable surface structure of  $\alpha$ - $\text{Fe}_2\text{O}_3$ (0001), i.e., the actual catalytically active phase.

## 4. Experimental Section

**Sample Preparation:** Natural  $\alpha$ - $\text{Fe}_2\text{O}_3$ (0001) single crystals were acquired from SurfaceNet GmbH. A total of ten crystals were used to carry out the experiments. Each crystal had a different concentration and elemental composition of impurities; the ones found were: Na, Ca, K, Mn, Zn, In, Ti, Mo, Cr, Al, and Sr. The amount and type of impurities detected at the surface were found to depend on the preparation conditions and sample history (sputtering and annealing cycles and oxygen partial pressure). It was important to note that impurity concentrations as low as 0.2 at.% could induce the formation of ferrite spinel structures.<sup>[31]</sup>

To reduce the samples into the magnetite phase,  $\alpha$ - $\text{Fe}_2\text{O}_3$ (0001) single crystals were sputtered with  $\text{Ar}^+$  (10 min,  $1 \times 10^{-6}$  mbar, 1–1.5 keV, 10 mA, 60  $\mu\text{A}$ ) and annealed in UHV (600–800 °C, 30 min) until a clear  $(1 \times 1)$  magnetite LEED diffraction pattern was observed with no hematite diffraction spots. The honeycomb phase was obtained by oxygen annealing ( $1 \times 10^{-6}$  mbar, 500–800 °C, 1–8 h) until no magnetite phase was detected by LEED. The  $(1 \times 1)$  phase was obtained on natural crystals after producing the honeycomb by oxygen annealing ( $1 \times 10^{-5}$  mbar of  $\text{O}_2$ , 500 °C, 30 min). The annealing was performed by radiative heating from a hot filament (Ta) and a temperature increase of 50–100 °C  $\text{min}^{-1}$  to avoid sample cracking. During the measurements, the samples were regularly refreshed by a 10–20 min oxygen annealing ( $1 \times 10^{-6}$  mbar, 600 °C) to remove adventitious carbon contamination. Two crystals were heavily contaminated by bulk dopants and it was not possible to reoxidize the magnetite phase.

**Synthetic Film Growth:** Synthetic hematite was obtained by PLD in a dedicated setup with in-UHV transfer to a dedicated surface-science chamber.<sup>[50]</sup> Films of roughly 100 nm thickness were grown on natural  $\alpha$ -

$\text{Fe}_2\text{O}_3$ (0001) single crystals from a single-crystalline  $\text{Fe}_3\text{O}_4$  target (700 °C,  $2 \times 10^{-2}$  mbar  $\text{O}_2$ , 5 Hz, 2.0 J  $\text{cm}^{-2}$ , no post-annealing, 60 °C  $\text{min}^{-1}$  ramp rate), as detailed elsewhere.<sup>[51]</sup> Before the growth, the natural samples were cleaned by repeated sputtering-annealing cycles (10 min,  $1 \times 10^{-6}$  mbar  $\text{Ar}^+$ , 1 keV; 30 min, 600 °C,  $1 \times 10^{-6}$  mbar  $\text{O}_2$ ) till no change in the contaminant signals was visible in XPS. Then, the samples were annealed at 850 °C for 1 h at  $2 \times 10^{-2}$  mbar  $\text{O}_2$ , to promote the flattening of the surface morphology and ensure complete oxidation of the crystals. The cleanliness of the films was checked by LEED and XPS.

**XPS, LEED, STM, and nc-AFM Characterization:** Normal emission XPS measurements were carried out using a laboratory-based system (SPECS Surface Nano Analysis GmbH, monochromatized Al-K $\alpha$  source) with a base pressure of  $5 \times 10^{-10}$  mbar. The core-level spectra were recorded with a pass energy of 20 eV, step size of 0.05 eV, and dwell time of 200 ms. No charging was observed. LEED patterns were acquired with SPECS Er-LEED 150 setups. The LEED apparatus was under operation parameters for at least 1 h before transferring the samples to avoid contamination (C, F). High-energy (150–300 eV) electrons were used to probe traces of the magnetite phase below the surface layers. Room-temperature STM images were acquired in several STM apparatuses with electrochemically etched W tips. The tips were treated on Au(111) before measuring hematite. Non-contact AFM images were acquired in an Omicron POLAR-SPM microscope at 78 K using Qplus sensors (resonance frequency of ca. 47 kHz, Q factor of ca. 5000) with an electrochemically etched W tip. The tip was prepared on Cu(100) until a change in the resonance frequency  $< -1.5$  Hz at 0.1 V bias was obtained while approaching the tip, and the contact potential difference between tip and sample was  $< 0.2$  V.

**Data Processing:** XPS data was processed using the KolXPD software. The binding energy positions were calibrated using the Fermi edge measured on a Ta sample plate. LEED images were acquired by averaging for 10 s with a camera in a dark receptacle. Dark-field images were acquired by turning off the LEED-screen acceleration voltage. They were subtracted from the original data to remove stray light and filament reflections. The contrast of the images was inverted to enhance the diffraction pattern. The STM and nc-AFM images were processed using custom ImageJ plug-ins. Microscope noise frequencies were filtered out. The lattice parameters of the honeycomb phase were obtained by dividing the distance between two spots containing 10–15 atomic positions by the number of unit cells. This was repeated in several locations in the three crystallographic directions to account for scanning distortions. The error bars corresponded to the standard deviation of these measurements. The figures were prepared using ImageJ, Gimp, and Inkscape.

**TEM Lamella Fabrication and Measurements:** The samples were covered by an Ag layer in the same UHV system where the samples were prepared. This protective cap prevents contamination of the topmost surface layers as a result of exposure to ambient conditions. Additionally, it prevents the surface from coming in direct contact with the reactive layers deposited during the lamella fabrication. Ag was deposited by thermal evaporation from a Knudsen-type effusion cell (crucible at 850 °C). The sample was held at room temperature in front of the effusion cell for 78 min, resulting in a  $\approx 30$  nm-thick Ag film. The pressure in the chamber during deposition was  $4 \times 10^{-10}$  mbar. Afterward, the sample was removed from UHV.

As the first step of the lamella fabrication, a protective cap ( $\approx 350$  nm thick) was deposited using electron-beam-induced deposition (EBID), followed by ion-beam-induced deposition (IBID) of the same element. Several gas injection system (GIS) chemistries for the deposition were tested (C, Pt, W): W or Pt did not introduce unwanted species into the layers of interest. The deposition of C makes it difficult to restore the sample for UHV experiments and causes extensive deposition of carbonaceous layers during TEM/EELS measurements, which are detrimental to the quality of results. The lamella was then liberated from the bulk by FIB milling with 30 keV Ga ions and transferred onto a Cu support grid. In order to suppress carbon contamination of the lamella as much as possible, the FIB-SEM chamber was plasma-cleaned before inserting the bulk sample. Two final thinning and polishing steps were conducted at 5 and 2 keV beam energies, respectively. In this study, the TEM lamella surface was normal w.r.t. the  $[11\bar{2}0]$  direction of bulk hematite.



The TEM measurements were performed at an accelerating voltage of 300 kV with a microscope TITAN Themis 60–300 (ThermoFisher Scientific) equipped with a monochromator and a spherical aberration ( $C_s$ ) corrector of objective lens. The HRTEM images were acquired with  $C_s \approx 0 \mu\text{m}$  and with an appropriate defocus in range of few nm to observe atomic columns with minimum delocalization. Velox software v.2.12 was used for the image acquisition and processing of corresponding FFT patterns used for crystallographic evaluation.

The STEM-EELS measurements were performed with a Quantum ERS spectrometer (Gatan) using an electron probe with current  $\approx 100 \text{ pA}$  and a convergence semi-angle of 10 mrad, a collection semi-angle of 28.2 or 56.4 mrad, and an entrance aperture of 2.5 or 5 mm, respectively. The EELS datasets were obtained with GMS v.3.3 software with enabled Dual-EELS mode allowing a simultaneous collection of a low-loss spectrum image and a high-loss spectrum image containing a zero-loss peak and edges of elements of interest, respectively, in each pixel. The used pixel size (i.e., the spatial resolution) and pixel time of the high-loss spectrum images were 0.3–0.5 nm and 0.02–0.08 s, respectively. The EELS data of Fe- $L_{3,2}$  fine-edge structure was acquired in monochromated STEM and with electron energy dispersion of 0.025 eV per channel giving an energy resolution  $\approx 0.12 \text{ eV}$ . The EELS data for chemical concentration measurements and elemental mapping were performed with dispersion of 0.25 or 0.5 eV per channel. Relative chemical concentrations were calculated in At. % by using a model-based EELS quantification function included in the GMS 3, where the following settings were chosen with emphasis on the best fit with the obtained spectra: signal sum width was selected within extended energy-loss fine structure part of particular edges, no overlap of edges was selected, background subtraction was performed with a Power Law model (for Fe- $L$  and O- $K$  edge) and a first Order Log-Polynomial model (for Mn- $L$  edge), the cross-section was calculated with a Hartree–Slater model and plural scattering was deconvoluted from high-loss spectrum images with the use of corresponding low-loss spectrum images. The Fe- $L_{3,2}$  fine-edge structure analysis was performed after the background subtraction by the Power Law model and plural scattering deconvolution by a Fourier-Ratio method.

## Supporting Information

Supporting Information is available from the Wiley Online Library or from the author.

## Acknowledgements

J.R. acknowledges support from the Grant Agency of Charles University (GAUK) and Czech Republic (GAČR) projects number 160119 and 22–180790, respectively. G.F. and U.D. were supported by the European Research Council (ERC) under the European Union's Horizon 2020 research and innovation program, grant agreement No. 883395, Advanced Research Grant “WatFun”. G.S.P. and F.K. were supported by the ERC under the European Union's Horizon 2020 research and innovation program, grant agreement No. 86462, Consolidator Research Grant “E-SAC”. Part of the research was carried out using the CzechNanoLab Research Infrastructure supported by MEYS CR (LM2018110). N.K. acknowledges Grant CEITEC VUT-K-22-7782, realized within the KInG BUT scheme No. CZ.02.2.69/0.0/0.0/19\_073/0016948, financed from the OP RDE. M.B. acknowledges financial support through the ERC and MEYS CR co-funded IMPROVE V project CZ.02.01.01/00/22\_010/0002552. M.Sv. acknowledges CzechNanoLab Research Infrastructure supported by MEYS CR (LM2023051). M.R. acknowledges support from the Austrian Science Fund (FWF) through project SFB-F81 “Taming Complexity in materials modeling” (TACO). The authors thank Michael Schmid for providing ImageJ plug-ins.

## Conflict of Interest

The authors declare no conflict of interest.

## Data Availability Statement

The data that support the findings of this study are available from the corresponding author upon reasonable request.

## Keywords

iron oxide, nc-AFM, surface structure, TEM, XPS

Received: July 12, 2023  
Published online: August 18, 2023

- [1] G. S. Parkinson, *Surf. Sci. Rep.* **2016**, 71, 272.
- [2] A. G. Tamirat, J. Rick, A. A. Dubale, W. N. Su, B. J. Hwang, *Nanoscale Horiz.* **2016**, 1, 243.
- [3] J. Deng, Q. Zhang, X. Lv, D. Zhang, H. Xu, D. Ma, J. Zhong, *ACS Energy Lett.* **2020**, 5, 975.
- [4] A. Kay, D. A. Grave, D. S. Ellis, H. Dotan, A. Rothschild, *ACS Energy Lett.* **2016**, 1, 827.
- [5] K. Sivula, F. Le Formal, M. Grätzel, *ChemSusChem* **2011**, 4, 432.
- [6] C. Li, Z. Luo, T. Wang, J. Gong, *Adv. Mater.* **2018**, 30, 1707502.
- [7] A. Bard, F. R. F. Fan, A. Gioda, G. Nagasubramanian, H. White, *Faraday Discuss. Chem. Soc.* **1980**, 70, 19.
- [8] L. Palmolahti, H. Ali-Löytty, R. Khan, J. Saari, N. V. Tkachenko, M. Valden, *J. Phys. Chem. C* **2020**, 124, 13094.
- [9] J. Li, W. Wan, C. A. Triana, H. Chen, Y. Zhao, C. K. Mavrokefalos, G. R. Patzke, *Nat. Commun.* **2021**, 12, 255.
- [10] J. Qiu, H. Hajibabaei, M. R. Nellist, F. A. L. Laskowski, S. Z. Oener, T. W. Hamann, S. W. Boettcher, *ACS Energy Lett.* **2018**, 3, 961.
- [11] X. Zhang, C. Cao, A. Bieberle-Hütter, *J. Phys. Chem. C* **2016**, 120, 28694.
- [12] A. J. E. Rettie, W. D. Chemelewski, D. Emin, C. B. Mullins, *J. Phys. Chem. Lett.* **2016**, 7, 471.
- [13] T. J. Smart, Y. Ping, *J. Phys. Condens. Matter* **2017**, 29, 394006.
- [14] E. Pastor, J. S. Park, L. Steier, S. Kim, M. Grätzel, J. R. Durrant, A. Walsh, A. A. Bakulin, *Nat. Commun.* **2019**, 10, 3962.
- [15] C. X. Kronawitter, I. Zegkinoglou, S. H. Shen, P. Liao, I. S. Cho, O. Zandi, Y. S. Liu, K. Lashgari, G. Westin, J. H. Guo, F. J. Himpsel, E. A. Carter, X. L. Zheng, T. W. Hamann, B. E. Koel, S. S. Mao, L. Vayssieres, *Energy Environ. Sci.* **2014**, 7, 3100.
- [16] H. Zhang, J. H. Park, W. J. Byun, M. H. Song, J. S. Lee, *Chem. Sci.* **2019**, 10, 10436.
- [17] G. Ketteler, W. Weiss, W. Ranke, R. Schlögl, *Phys. Chem. Chem. Phys.* **2001**, 3, 1114.
- [18] G. Ketteler, W. Weiss, W. Ranke, *Surf. Rev. Lett.* **2001**, 8, 661.
- [19] S. K. Shaikhutdinov, Y. Joseph, C. Kuhrs, W. Ranke, W. Weiss, *Faraday Discuss.* **1999**, 114, 363.
- [20] M. Pollak, M. Gautier, N. Thromat, S. Gota, W. C. Mackrodt, V. R. Saunders, *Nucl. Instrum. Methods Phys. Res. B* **1995**, 97, 383.
- [21] C. Y. Kim, A. A. Escudero, M. J. Bedzyk, L. Liu, P. C. Stair, *Surf. Sci.* **2004**, 572, 239.
- [22] N. G. Condon, F. M. Leibsle, A. R. Lennie, P. W. Murray, D. J. Vaughan, G. Thornton, *Phys. Rev. Lett.* **1995**, 75, 1961.
- [23] H. Qiu, V. Staemmler, H. Kühlenbeck, E. Bauer, H. J. Freund, *Surf. Sci.* **2015**, 641, 30.
- [24] H. Qiu, H. Kühlenbeck, E. Bauer, H. J. Freund, *J. Phys. Chem. C* **2019**, 123, 8221.
- [25] R. J. Lad, V. E. Henrich, *Surf. Sci.* **1988**, 193, 81.
- [26] C. H. Lanier, A. N. Chiamonti, L. D. Marks, K. R. Poeppelmeier, *Surf. Sci.* **2009**, 603, 2574.



- [27] J. Redondo, P. Lazar, P. Procházka, S. Průša, B. Mallada, A. Cahlík, J. Lachnitt, J. Berger, B. Šmíd, L. Kormoš, P. Jelínek, J. Čechal, M. Švec, *J. Phys. Chem. C* **2019**, 123, 14312.
- [28] G. Franceschi, M. Wagner, J. Hofinger, T. Krajňák, M. Schmid, U. Diebold, M. Riva, *Phys. Rev. Mater.* **2019**, 3, 103403.
- [29] S. A. Chambers, Y. J. Kim, Y. Gao, *Surf. Sci. Spectra* **1998**, 5, 219.
- [30] J. H. Paterson, O. L. Krivanek, *Ultramicroscopy* **1990**, 32, 319.
- [31] A. N. Chiaramonti, P. C. Stair, L. D. Marks, *Surf. Sci.* **2005**, 586, 38.
- [32] F. Kraushofer, Z. Jakub, M. Bichler, J. Hulva, P. Drmota, M. Weinold, M. Schmid, M. Setvin, U. Diebold, P. Blaha, G. S. Parkinson, *J. Phys. Chem. C* **2018**, 122, 1657.
- [33] G. Franceschi, F. Kraushofer, M. Meier, G. S. Parkinson, M. Schmid, U. Diebold, M. Riva, *Chem. Mater.* **2020**, 32, 3753.
- [34] M. Lewandowski, Scanning Tunneling Microscopy Study of Iron Oxide Based Model Catalysts, **2011**, 10.14279/depositon-2974.
- [35] J. W. Elam, C. E. Nelson, M. A. Cameron, M. A. Tolbert, S. M. George, *J. Phys. Chem. B* **1998**, 102, 7008.
- [36] F. Kraushofer, G. S. Parkinson, *Chem. Rev.* **2022**, 122, 14911.
- [37] T. Ossowski, T. Pabisia, A. Kiejna, K. Palotás, E. Bauer, *J. Phys. Chem. C* **2021**, 125, 26711.
- [38] S. H. Cheung, A. Celik-Aktas, P. Dey, K. Pande, M. Weinert, B. Kabius, D. J. Keavney, V. K. Lazarov, S. A. Chambers, M. Gajdardziska-Josifovska, *Phys. Rev. B – Condens. Matter Mater. Phys.* **2012**, 85, 045405.
- [39] H. S. C. O'Neill, W. A. Dollase, *Phys. Chem. Miner.* **1994**, 20, 541.
- [40] L. W. Finger, R. M. Hazen, *J. Appl. Phys.* **1980**, 51, 65.
- [41] S. Y. Chen, A. Gloter, A. Zobelli, L. Wang, C. H. Chen, C. Colliex, *Phys. Rev. B – Condens. Matter Mater. Phys.* **2009**, 79, 104103.
- [42] T. P. Almeida, T. Kasama, A. R. Muxworthy, W. Williams, L. Nagy, T. W. Hansen, P. D. Brown, R. E. Dunin-Borkowski, *Nat. Commun.* **2014**, 5, 5154.
- [43] A. Sala, H. Marchetto, Z. H. Qin, S. Shaikhutdinov, T. Schmidt, H. J. Freund, *Phys. Rev. B – Condens. Matter Mater. Phys.* **2012**, 86, 155430.
- [44] B. Mallada, S. Edalatmanesh, P. Lazar, J. Redondo, A. Gallardo, R. Zbořil, P. Jelínek, M. Švec, B. De La Torre, *ACS Sustainable Chem. Eng.* **2020**, 8, 3437.
- [45] J. Goniakowski, F. Finocchi, C. Noguera, *Reports Prog. Phys.* **2008**, 71, 016501.
- [46] S. A. Chambers, S. I. Yi, *Surf. Sci.* **1999**, 439, L785.
- [47] S. Yamamoto, T. Kendelewicz, J. T. Newberg, G. Ketteler, D. E. Starr, E. R. Mysak, K. J. Andersson, H. Ogasawara, H. Bluhm, M. Salmeron, G. E. Brown, A. Nilsson, *J. Phys. Chem. C* **2010**, 114, 2256.
- [48] A. N. Chiaramonti, Structure and Thermodynamics of Model Catalytic Oxide Surfaces, **2005**, [http://www.numis.northwestern.edu/thesis/chiaramonti\\_abstract.html](http://www.numis.northwestern.edu/thesis/chiaramonti_abstract.html).
- [49] P. Liao, E. A. Carter, *J. Appl. Phys.* **2012**, 112, 013701.
- [50] S. Gerhold, M. Riva, B. Yildiz, M. Schmid, U. Diebold, *Surf. Sci.* **2016**, 651, 76.
- [51] G. Franceschi, M. Schmid, U. Diebold, M. Riva, *Rev. Sci. Instrum.* **2020**, 91, 065003.